

Local shear signals propagate to suppress local cellular motion in stiff epithelia

Shahar Nahum¹, Adi Y. Elkabetz¹, Matan Elbaz¹, Liav Daraf¹, Yael Lavi¹, Lior Atia^{1*}

¹Department of Mechanical Engineering; Ben-Gurion University of the Negev, Beer-Sheva 8410501, Israel; *atalior@bgu.ac.il

Abstract

As small particles skim our airways during breathing, or our intestines during digestion, the surface epithelium is subjected to local exogenous shear that deforms hundreds to thousands of tightly interacting cells. Unlike shear deformations applied at the macro-tissue scale or the micro-cell scale, the effects of such perturbations at the meso-scale remain largely unexplored. To address this, we developed a mesoscopic probe that adheres to the apical surface of an epithelial monolayer and applies magnetically derived local shear. We find that localized shear propagated way beyond immediate neighbors and suppressed cellular migratory dynamics in stiffer layers, yet dissipated locally and left dynamics unchanged in softer layers. This mechano-transductive view is reinforced by the observation that stiffening of a soft layer promotes responsiveness to shear. Interpreted within the epithelial jamming framework, shear-induced migratory suppression in stiff layers was accompanied by reduced MSD scaling exponents and changes in cell shape. These changes suggested a localized shift of the tissue toward a lower-energetic state. Together, these observations provide a new perspective on how a local mechanical perturbation traverses the epithelial monolayer to influence both nearby and distant cellular environments.

Significance

Epithelial tissues are routinely exposed to localized mechanical shear, arising from particles or perturbing objects. While the effects of shear forces acting at single-cell or whole-tissue scales are well-studied, how localized perturbations influence collective epithelial behavior is unclear. Here, we show how local shear suppresses cellular motion, a process that depends critically on epithelial rigidity. In mechanically stiff epithelia, localized shear propagates across many cell rows and broadly suppresses cellular dynamics, whereas in softer epithelia, the same perturbation dissipates locally and has little effect. These findings reveal epithelial rigidity as a key mechanical filter that determines whether local shear perturbations that might be stemming from an inhaled particle, or an emerging tumor, remain confined or propagate to reorganize collective behavior.

Main text

Introduction

Epithelial layers line organs, maintain barrier function, and actively remodel during development, homeostasis, and repair. While doing so, they experience mechanical shear forces acting along multiple size scales. Large tissue-level shear deformations that occur during morphogenesis, breathing, or peristalsis were studied using various whole-tissue stretching assays, showing fundamental growth-related pathways¹⁻³, and mechanical fracturing characteristics^{4,5}. Small cell-level shear deformations that occur during immune extravasation⁶, mitosis^{7,8}, or extrusion⁹, were studied using subcellular perturbations and were shown to affect cell adhesion¹⁰, cytoskeleton organization¹¹, and even promote intracellular fluid-like microrheology¹²⁻¹⁴. However, between these regimes lies an unexplored mesoscale domain, in which, for example, exogenous particles in the lung or in the intestines apply locally concentrated shear forces that deform hundreds to a few thousand of tightly interacting epithelial cells. Mesoscale forces have been studied in the developing mesoderm^{15,16}, however, how such mesoscale shear propagates across the adherent epithelial monolayer, and how it contributes to local mechanotransduction in relevant physiological contexts, remains largely unknown¹⁷.

To fill this gap, we developed a mesoscopic magnetic probe that adheres to the epithelial apical surface and applies controlled lateral shear to living monolayers. By characterizing local cellular dynamics and rheological properties, we demonstrate how the shear response traverses outwards from the perturbing site in an unexpected manner, and that it depends critically on local tissue rigidity. These results identify mechanical malleability as a key parameter governing the spatial reach of shear-induced signals and establish localized shear as a distinct mode of multicellular communication.

Local mechanical shear suppresses cellular motion in nearby cells

To examine how local mesoscale perturbations affect epithelial behavior, we established an assay that applies controlled mechanical shear to confined epithelial monolayers. The system consists of a maturing tissue of Madin-Darby Canine Kidney (MDCK) epithelial cells, cultured within physical confinement and allowed to mature for three distinct durations: right as the layer becomes confluent (t0); 5 hours post-confluence (t5); and 10 hours post-confluence (t10). We used a mixture of polydimethylsiloxane and iron oxide (PDMS-Fe) to create a magnetizable disc. The disc was placed directly atop the monolayer (Fig. 1a,c; Methods; Supplementary Fig. 1), and a magnetic tweezer setup was used to apply a lateral force of approximately 2×10^4 nN (Fig. 1b; Methods; Supplementary Fig. 2), generating a 10s duration localized shear (Supplementary Video 1; Methods). As a control, we prepared matched samples with attached magnetic discs but without applying any force. Monolayers were then imaged using time-lapse to capture cells migratory response. This design enabled us to examine how maturation and localized shear influence the mechanical and dynamic properties of epithelial tissues surrounding the perturbed site. Surprisingly, unlike studies applying tissue-scale deformations^{18,19}, our localized shear caused motility to fall well below that of unperturbed tissues, marking a pronounced suppression of migration (Supplementary Video 2). That migratory suppression was observed far beyond the disc in the t0 and t5 tissues (Fig. 1d-e; Methods). In contrast, the more mature t10 tissues showed no comparable reduction in motion, as mean velocity remained unchanged between sheared and control samples. This observed

relationship between tissue maturation and its dynamic responsiveness to shear prompted us to consider whether this is due to progressive mechanical stiffening.

Maturation-dependent softening restrains the transmission of mechanical shear signals

To explore the idea that maturation alters tissue mechanical responsiveness, we quantified the shear strain γ generated within the epithelial layer, directly beneath the magnetic disc. This required measuring the epithelial height at each maturation stage, and tracking the displacement of the disc during the shear (Fig. 2a–b; Methods; Supplementary Fig. 4). The strong motility suppression in t0 and t5, and the absence of this response in t10, initially led us to hypothesize that the less mature tissue was compliant and softer, whereas the more mature tissue was incompliant and stiffer. Unexpectedly, the strain measurements revealed the opposite. The less mature tissues showed substantially lower strain than the mature tissues, identifying the most mature ones as the softest (Fig. 2c; Supplementary Table 1). This result indicates that, under the prescribed spatial constraints (Fig. 1a), maturation leads to a tissue softening transition. Notably, since t0 and t5 experience comparable strains, that transition is not progressive but rather abrupt (Fig. 2c).

Stiffness or rigidity of biological cells is commonly assessed using the power-law rheology model, $\gamma(t) \propto t^\beta$, where β typically ranges from 0.1 to 0.5, with smaller values indicating stiffer behavior^{11,14}. We therefore examined whether the β exponent would reflect the softening we observed. Fitting the strain curves (Supplementary Fig. 5) to the power-law model yielded two key findings. First, during monolayer recovery after shearing, β values markedly decreased, but in a manner that was independent of tissue maturation (Fig. 2d). This behavior is consistent with previous reports showing that external forces transiently fluidize the cytoskeleton¹². Second, β remained essentially unchanged throughout all maturation times (Fig. 2d). Thus, the maturation-dependent softening we observe is not captured by the exponent β .

The overall effects of local shear deformations act to suppress cellular dynamics many cell rows far from the perturbed site in the less mature tissue (Fig. 1d; Supplementary Video 2). Yet, this less mature tissue also undergoes small shear-induced deformations. Taken together, the observations lead to a striking paradox. If the extent of deformation were the primary determinant of the long-range suppression of cellular dynamic, one would expect the most strained tissue (t10; Fig. 2c) to show the strongest long-range effect. Instead, we observe the opposite: in the less mature tissues (t0 and t5), motility suppression propagates over large distances, while in most mature tissues (t10), it barely propagates at all (Fig. 1d). This counterintuitive behavior raises the possibility of a distinct physical mechanism. Analogous to pressure waves traveling farther in more rigid materials, could shear-induced signals travel farther to suppress migration across a stiffer epithelial monolayer?

Induced migration promotes shear responsiveness

Exploring this idea might require a more detailed mapping of spatial stiffness. We lacked, however, the technology to precisely control the micro-level placement of the magnetic disc. Nevertheless, we were able to gain an initial clue by plotting the stiffness measurements obtained from randomly placed discs against their distance from the tissue edge (Fig. 3a). We found that stiffness gradually decreased with increasing distance from the tissue boundary. This observation made us consider a possible connection to the well-known phenomenon in which migration velocity is generally higher near the free tissue boundary²⁰ (Fig. 3b). It led us to

hypothesize that enhancing cellular migration within the t10 tissue could act to stiffen it and thereby restore its susceptibility to shear-induced migratory suppression.

We therefore performed a complementary set of experiments in which, immediately after confluence, we removed the physical barrier confining the monolayer in order to promote cellular migration (Fig. 3c; Methods). We then waited either 5h or 10h, applied the same shear protocol as before to these unconfined tissues, and measured the rheological response. The resulting strain curves followed a clear power-law, yielding β values that closely matched those of confined tissues (Fig. 3d). Furthermore, similar to the confined monolayers, during recovery after shearing of the unconfined monolayers, the β values consistently dropped (Fig. 3d). That is, no behavioral changes were captured by the exponent β for unconfined monolayers. However, shear strains in the unconfined monolayers were substantially lower than those in their confined counterparts (Fig. 3e). This reduction supported our hypothesis and demonstrated that unconstrained maturation promotes a mechanically stiffer phenotype. While confined t10 tissues showed no detectable change in mean cellular motility following shear (Fig. 1), unconfined t10 tissues did respond to shear and displayed a clear motility suppression (Fig. 3f). Together, these findings demonstrate that lifting spatial constraints promotes both stiffness and shear-signal propagation, strengthening the idea that mechanical cues transmit more effectively in stiffer monolayers.

Previous studies have shown that processes such as wound healing or stimulated migration can trigger cell-cycle reentry and increased proliferation^{19,21}. We therefore asked whether the enhanced dynamics and applied shear in unconfined tissues might have induced cell division, potentially contributing to the observed mechanical changes (Fig. 3). Using a cell cycle fluorescence reporter^{19,22}, we quantified cell-cycle states in both perturbed and unperturbed conditions²³ (Methods). We detected no measurable differences in cell-cycle progression, indicating that the mechanical perturbation did not affect proliferation and is therefore unlikely to account for the observed behaviors in unconfined tissues (Supplementary Fig. 6).

Shear-induced migratory suppression partially coincides with jamming metrics

To gain a deeper physical understanding of our observations, we turned to a theoretical framework inspired by concepts from granular and soft glassy systems²⁴, known as multicellular jamming. This framework has emerged in biophysics as a way to elucidate observed epithelial transitions from an unjammed fluid-like state with abundant cellular motion, to a jammed solid-like state with suppressed motion²⁵⁻³⁷. Since we also observed a shear-induced suppression of cellular motion, we wondered whether our observations are consistent with, and can be described by, dynamical and geometrical signatures identified with epithelial jamming.

Dynamically, the mean squared displacement (MSD) quantifies how far cells wander from their original positions over Δt time (Fig. 4a). MSD distinguishes between random diffusion, confined motion, and super-diffusive rearrangements^{32,36,37}. By fitting the MSD curves to a power-law model ($MSD(\Delta t) \propto t^\alpha$) we could extract the change in α parameter that reflects altered caging dynamics. By definition, $\alpha > 1$ reflects an uncaged dynamics, and reducing α values reflects an increasing caging (Fig. 4a). In most cases, applying local shear reduced the α values (Fig. 4b), and changes, or lack thereof, in α and cell velocity were in concordance (Fig. 3f). One exception, the unconfined t10 tissue, did not obey that relationship, as after applying shear α did not change, but cell velocity did drop. Nevertheless, in general, the

observations suggest that shear reduces the magnitude of cellular self-propulsion and that the collective pattern of motion transitions toward more caged dynamics. We then wondered whether we could support or refute this interpretation with other jamming metrics, namely geometrical.

Geometrically, a central metric in the jamming framework is cell shape, as formalized in the theoretical vertex model^{26,27,38}. In this model, multicellular jamming emerge from the balance between cell–cell adhesion and cortical tension, which are encoded in cell shape²⁶. Multiple studies corroborated the main prediction of the vertex model, showing that a transition from an unjammed state to a jammed state is reflected by a reduction in cell shape indices ($Perimeter/\sqrt{Area}$; Aspect Ratio)^{28,32-34,36,37}. In most of our observations, applying local shear reduced the cell shape values (Fig. 4c). However, in the unconfined t10 tissue, in which α did not change, but the velocity decreased, cell shape increased. This important exception might be reflecting missing unknown factors in the jamming framework.

Discussion

The results presented here establish a direct link between epithelial rigidity and the spatial reach of mechanically induced suppression of cellular dynamics. Local apical shear, when applied to a mechanically stiff epithelial layer (t0, t5, t5UC, t10UC; Fig. 2c and Fig. 3e) suppresses migration across many cell rows, propagating far beyond the site of perturbation. In contrast, the same shear perturbation dissipates locally in softer layers (t10; Fig. 2c), leaving cellular dynamics largely unchanged. These observations indicate that epithelial rigidity enables a coherent transmission of shear-derived signals across the monolayer.

All examined tissues exhibited relatively low MSD exponents and cell shape values to begin with^{32,46}, and, nevertheless, in most cases, after local shear, shape and motion reduced even further, and did so simultaneously. A unifying interpretation of our data is that all examined tissues reside within a jammed or near-jammed state, and that shear acts not to induce jamming per se, but rather suppresses residual cellular dynamics within an already mechanically constrained system. In this view, self-propulsion prior to shear serves as an active perturbation that sustains slight cellular motion and shape irregularity, keeping cells mechanically poised and responsive. Local shear suppresses this self-propulsion, thereby effectively shifting the tissue toward reduced motion and geometric regularization, consistent with a lower-energetic state.³⁰

This perspective reframes shear-induced migratory arrest not as a jamming transition, but as an energetic down-shift within a jammed collective. Importantly, mesoscale stiffness measurements reveal that reduced migratory behavior does not necessarily correspond to increased mechanical stiffness. In confined mature epithelia (t10), low motility coincides with a softer mechanical response. In unconfined mature epithelia, increased motility coincides with increased stiffness (t10UC). These findings demonstrate that the common intuition, drawn from granular and glassy materials, and according to which “more jammed implies stiffer”²⁴, does not hold in the epithelial monolayer.

Methods

Cell Culture and Experimental Groups

Madin-Darby Canine Kidney (MDCK) II epithelial cells (stably expressing either ZO-1 GFP⁴⁷, or the FUCCI transgene¹⁹) were used throughout this study. FUCCI Cells were a kind gift from Lars Hufnagel. Cells were maintained in Modified Eagle Medium (MEM) supplemented with 10% fetal bovine serum (FBS), 1% penicillin-streptomycin and 1% L-Glutamine, under standard culture conditions of 37°C, 5% CO₂, and 85% humidity. For each experiment, a 35 mm Petri dish was prepared by attaching a single Ibidi insert (Culture-Insert 2 Well cat#80209) near the dish's edge to allow proper access for the magnetic tweezer. The insert was either new or prewashed with ethanol prior to use. One of the wells was seeded with 56,000 cells in 70 µL. To prevent dehydration, 2 mL of additional medium was added around the well. Cells were cultured for defined durations prior to shear: t0 - 20 hours to reach confluence; t5 - 25 hours; t10- 30 hours. Two experimental groups were defined based on when the insert was removed: Unconfined (UC) group: The well was removed after 20 hours, allowing the tissue to expand freely; Confined group: Cells remained confined within the well throughout the growth period.

Preparation of Magnetic Discs

Magnetic discs used for pulling experiments were fabricated in-house using polydimethylsiloxane (PDMS; SYLGARD™ 184 Silicone Elastomer KIT, DOW) mixed with 10% (weight) iron oxide (Iron(II,III) oxide Fe₃O₄, Sigma-Aldrich, Cat# 637106) to allow magnetization. A PDMS mixture with the iron and 10% curing agent was prepared. The mixture was thoroughly mixed, degassed under vacuum for 10 minutes, and cast on ethanol-cleaned glass slides to a final thickness of ~500 µm. The thickness control was achieved by metallic spacers (filler gages; Amazon). After curing at 150°C for 10 minutes and cooling in room temperature, the PDMS was removed from the glass and cut into 750 µm diameter discs using a biopsy punch (Reuse Biopsy Punch, 0.75 mm, Cat# 504529, WPI).

Following fabrication, the PDMS-Fe discs underwent a multi-step surface treatment protocol to enhance adhesion to the epithelial tissue. Discs were first immersed in 70% ethanol and exposed to UV light for 30 minutes to sterilize and activate the surface. Next, the discs were washed three times with 3 mL of PBS. An Eppendorf tube containing the 20 µL SANPAH (Sulfo-SANPAH (sulfosuccinimidyl 6-(4'-azido-2'-nitrophenylamino) hexanoate, Moshe Shtauber) solution was thawed, then diluted with 980 µL of PBS and added to the beaker with the discs. The beaker was then placed under UV light for an additional 30 minutes to activate the crosslinking of SANPAH to the PDMS surface. After UV activation, the discs were washed with 3 mL PBS as many times as was necessary to render the beaker completely clean of SANPAH (the solution is completely clear).

For RGD coating, a 50 µg/mL RGD peptide (Arg-Gly-Asp, Sigma-Aldrich, Cat# A8052) stock solution in PBS was prepared. Of this solution, 200 µL were diluted with 3.8 mL PBS, and added to the beaker with the discs. Finally, the beaker with the discs and RGD solution was fixed to a shaker using aluminum tape and shaken at 370 RPM for 24 to 72 hours at room temperature.

Disc Placement and its Adhesion to the tissue

To allow for discs adherence to tissue, a permanent round magnet (Amazon 1.94 mm diameter, 0.96 mm thick) was taped to the underside of the dish at the desired location. Using tweezers, a disc was gently introduced into the medium above the magnet, allowing it to sink and adhere to the tissue, such that it was attracted solely by the magnet. After disc placement, samples were incubated for 30 minutes at 37°C, 5% CO₂, and 85% humidity to promote strong disc–tissue adhesion.

Local shearing

To apply local shear forces, the culture well and the magnet were carefully removed. The sharp tip of the magnetic tweezer was positioned 500 µm from the disc and connected to a current supply set to 2A. 10 second duration force was applied on the disc, followed by 10 seconds recovery, producing 20-second videos that captured both deformation and relaxation phases of the tissue response (Supplementary video 1).

Microscopy

Long-term imaging (cellular migration)

To examine long-term responses of the tissue to local shear, time-lapse imaging was conducted following the shearing procedure. Real-time imaging was carried out on a ZEISS AXIO OBSERVER 7 microscope, equipped with an environmental control chamber (maintained at 37°C, 5% CO₂, and 85% humidity), and an AXIOMONOCAM 712 MONO camera. Samples were placed under incubation-controlled conditions and imaged every 10 minutes for 3 to 5 hours.

Short-term imaging (mesoscale rheology)

Short-term imaging was performed using a ZEISS AXIO VERT.A1 microscope equipped a AXIOMONOCAM 202 MONO camera. Shear experiments were imaged in real time at 31 frames per second. Imaging was performed in both phase contrast and fluorescence modes, allowing precise observation of cell boundaries and tissue morphology.

Optical Sectioning imaging

Tissues were fixed and stained for actin (alexa 647-phalloidin). Z-stacks were obtained using ZEISS AXIO OBSERVER 7 microscope equipped with an Apotome – a structured illumination module - to obtain optical sectioning of the tissue.

Tissue Height Measurements

Z-stacks were processed using the 3D Viewer tool in Fiji, allowing visualization of the actin-labeled cell architecture along the apical–basal axis. To quantify tissue height, four representative slices were selected from each sample, and the vertical extent of individual cells was measured manually using the PlotDigitizer (free version) software.

Image Velocimetry

To analyze tissue deformation and flow fields, we used TPIV (Time-resolved Particle Image Velocimetry), a Fiji plugin⁴⁸. PIV was performed on phase contrast images to calculate motion vector fields, including direction and magnitude of local movements. Data included vector

length, direction (angle), and terminal positions, allowing speed measurements throughout the experiment.

Actin staining

To visualize actin structures and measure epithelial tissue height, samples were fixed with 4% paraformaldehyde (Formaldehyde Solution, 16% (w/v), Thermo Scientific, Cat# 28908 diluted one ampule in 30ml PBS), permeabilized with 0.1% Triton X-100 (Triton X-100, 1% stock solution, Rhenium, Cat# HFH10Triton or X-100, 10% stock solution, Rhenium, Cat# TS-28314) and blocked using 1% BSA (Bovine Serum Albumin, Reagent Grade, Millipore, Cat# 81-066-4) in PBS. F-actin was then stained with Alexa Fluor 647-conjugated phalloidin (Rhenium, A22287), incubated for 60 minutes at room temperature in darkness, and subsequently washed with PBS. All samples were stored in PBS at 4°C, protected from light, and imaged within 1 to 2 weeks.

Segmentation and Tracking

Segmentation of the discs was performed using the Pixel Classification workflow in Ilastik (v3.4.3). The classifier was trained on several representative frames to distinguish between disc and cellular regions. The resulting probability map was thresholded in ImageJ using the “Make Binary” tool with auto-thresholding. A custom MATLAB script computed the disc displacement vector, assuming unidirectional movement.

For cell segmentation, Cellpose was employed to detect individual cells. The Cyto 2 model was used for phase contrast images. This enabled detailed analysis of morphology, including area, aspect ratio, and circularity. Cell tracking was performed using TrackMate (Fiji plugin), which is used for tracking labeled ROIs across frames, producing positional and morphological data for each cell.

Statistical Analysis

To determine statistical significance between experimental groups, we used the Mann-Whitney U test (also known as the Wilcoxon rank-sum test), a non-parametric method for comparing two independent samples. This test is appropriate for non-normally distributed data and is robust to outliers and heavy-tailed distributions, offering an efficient alternative to the t-test when the assumption of normality may not hold. The test was preformed using the built-in **ranksum** function in MATLAB.

Cell Cycle Analysis

To investigate the effect of mechanical perturbation on cell cycle progression, we performed time-lapse imaging following shear experiments, with FUCCI-expressing MDCK cells¹⁹, under the Unconfined (UC) condition. The FUCCI (Fluorescent Ubiquitination-based Cell Cycle Indicator) system enables real-time visualization of cell cycle dynamics in living cells through a dual-color reporter: nuclei appear red in the G1 phase and transition to green during S/G2/M phases²². This approach allows spatiotemporal monitoring of cell cycle progression in individual cells during tissue deformation.

Time-lapse imaging was conducted under the same environmental and optical conditions described previously, capturing cell behavior over several hours following the mechanical

perturbation. To analyze cell cycle progression, we used ConfluentFUCCI²³, an open-source GUI-based framework specifically developed for automated analysis of highly confluent and dynamic epithelial monolayers. These outputs were post-processed using a custom MATLAB script to identify the time points (frames) at which individual cells transitioned from red to green/yellow, indicating progression from G1 to S phase. This enabled quantitative assessment of how many cells advanced through the cell cycle during the experiment, and whether this progression was affected by the applied mechanical stress.

Magnetic Tweezer

The magnetic tweezer was fabricated from a 100 mm long high-permeability ST37 low-carbon steel core, comprising a 70 mm cylindrical section and a CNC-sharpened conical tip with a 16° angle. The core was wound with 350 turns of 0.50-mm insulated copper wire, which was subsequently covered with insulating tape.

Magnetic force was calculated by pulling individual discs through PDMS and converting their measured kinematics into forces using a force balance. Discs were positioned 1 mm from a horizontally mounted magnetic tweezer and imaged while being pulled toward the tweezer tip. Disc trajectories were extracted using FIJI and MATLAB, and forces were computed from the measured velocities using a constant drag coefficient. The drag coefficient was independently determined by analyzing the sinking motion of identical discs in PDMS at 20 °C. Disc kinematics were extracted using FIJI and MATLAB, and assuming force balance at steady state and a disc mass of 0.2 mg. Measurements from 26 discs yielded an average drag coefficient of $C_D = 5 \times 10^6$. The resulting force–distance relationships were fitted to exponential functions and corrected for the 45° tweezer angle used in tissue experiments (Supplementary Fig. 2).

MSD calculation

Mean squared displacement (MSD) analysis was performed to quantify spatial patterns of cell motility across experimental groups. Cell trajectories were obtained from TrackMate outputs, which provided the (x,y) centroid positions of individual cells in each frame. For each trajectory, MSD values were computed for increasing time lags Δt according to the standard definition:

$$MSD(\Delta t) = \langle [x(t + \Delta t) - x(t)]^2 + [y(t + \Delta t) - y(t)]^2 \rangle_t$$

where t denotes averaging over time. MSD was calculated up to a maximum lag of 180 minutes. Tracks shorter than 5 frames were excluded from the analysis. For each condition, MSD curves were computed for all individual tracks.

To characterize the mode of transport, the MSD curve of each individual track was fitted to a power-law model:

$$MSD(\Delta t) \propto (\Delta t)^\alpha$$

The exponent α serves as an indicator of the motion type. Due to the non-normal distribution of exponents across the population, the median exponent was utilized as the primary metric for central tendency. To estimate the uncertainty of these population medians, non-parametric bootstrap resampling was performed. For each experimental condition, the distribution of α values were resampled 1,000 times with replacement to generate a bootstrap distribution of the

median using MATLAB *bootci* function⁴⁹. The error bars are the resulting 95% confidence intervals (CI) of the median.

Acknowledgements

L.D acknowledges financial support from the Israel Scholarship Education Foundation (ISEF). L.A acknowledge financial support by the Israeli Science Foundation (ISF) on the individual research grant number 2107/21, and the New-Faculty Equipment grant number 2108/21; Israeli Ministry of Innovation, Science and Technology 0357- 24; BGU's joint collaboration grant, Engineering Sciences and the Blaustein Institutes for Desert Research, 2025; Pearlston Center at BGU; Israeli Young Academy.

Author contributions

S.N and L.A. conceptualized the research. S.N., Y.L., and L.A. designed the experiments. S.N., A.E., and Y.L. performed the experiments. M.E., and L.A. designed and created the experimental system. S.N., A.E., and L.A. designed and performed all presented analyses. S.N., Y.L., L.D., and L.A. contributed to data interpretation. S.N and L.A. wrote the manuscript. L.A oversaw the project.

Competing interest statement

Authors declare that they have no competing interests.

Data sharing

Data will be shared upon reasonable request from the corresponding author.

This PDF file includes:

- Main Text
- Figures 1 to 4
- Supplementary Figures 1 to 6
- Supplementary Tables 1
- Supplementary Videos 1 to 2 (referrals)

References

- 1 Gudipaty, S. A., Lindblom, J., Loftus, P. D., Redd, M. J., Edes, K., Davey, C. F., Krishnegowda, V. & Rosenblatt, J. Mechanical stretch triggers rapid epithelial cell division through Piezo1. *Nature* **advance online publication**, doi:10.1038/nature21407
<http://www.nature.com/nature/journal/vaop/ncurrent/abs/nature21407.html#supplementary-information> (2017).
- 2 Benham-Pyle, B. W., Pruitt, B. L. & Nelson, W. J. Mechanical strain induces E-cadherin-dependent Yap1 and beta-catenin activation to drive cell cycle entry. *Science* **348**, 1024-1027, doi:10.1126/science.aaa4559 (2015).
- 3 Aragona, M., Panciera, T., Manfrin, A., Giulitti, S., Michielin, F., Elvassore, N., Dupont, S. & Piccolo, S. A Mechanical Checkpoint Controls Multicellular Growth through YAP/TAZ Regulation by Actin-Processing Factors. *Cell* **154**, 1047-1059, doi:<http://dx.doi.org/10.1016/j.cell.2013.07.042> (2013).
- 4 Duque, J., Bonfanti, A., Fouchard, J., Baldauf, L., Azenha, S. R., Ferber, E., Harris, A., Barriga, E. H., Kabla, A. J. & Charras, G. Rupture strength of living cell monolayers. *Nature Materials* **23**, 1563-1574, doi:10.1038/s41563-024-02027-3 (2024).
- 5 Casares, L., Vincent, R., Zalvidea, D., Campillo, N., Navajas, D., Arroyo, M. & Trepaut, X. Hydraulic fracture during epithelial stretching. *Nat Mater* **14**, 343-351, doi:10.1038/nmat4206
<http://www.nature.com/nmat/journal/v14/n3/abs/nmat4206.html#supplementary-information> (2015).
- 6 Huse, M. Mechanical forces in the immune system. *Nature Reviews Immunology* **17**, 679-690, doi:10.1038/nri.2017.74 (2017).
- 7 Uroz, M., Wistorf, S., Serra-Picamal, X., Conte, V., Sales-Pardo, M., Roca-Cusachs, P., Guimera, R. & Trepaut, X. Regulation of cell cycle progression by cell-cell and cell-matrix forces. *Nature Cell Biology* **20**, 646-654, doi:10.1038/s41556-018-0107-2 (2018).
- 8 Uroz, M., Garcia-Puig, A., Tekeli, I., Elosegui-Artola, A., Abenza, J. F., Marín-Llauradó, A., Pujals, S., Conte, V., Albertazzi, L., Roca-Cusachs, P., Raya, Á. & Trepaut, X. Traction forces at the cytokinetic ring regulate cell division and polyploidy in the migrating zebrafish epicardium. *Nature Materials*, doi:10.1038/s41563-019-0381-9 (2019).
- 9 Eisenhoffer, G. T., Loftus, P. D., Yoshigi, M., Otsuna, H., Chien, C.-B., Morcos, P. A. & Rosenblatt, J. Crowding induces live cell extrusion to maintain homeostatic cell numbers in epithelia. *Nature* **484**, 546-549, doi:<http://www.nature.com/nature/journal/v484/n7395/abs/nature10999.html#supplementary-information> (2012).
- 10 Wang, N., Butler, J. & Ingber, D. Mechanotransduction across the cell surface and through the cytoskeleton. *Science* **260**, 1124-1127, doi:10.1126/science.7684161 (1993).
- 11 Bonakdar, N., Gerum, R., Kuhn, M., Sporrer, M., Lippert, A., Schneider, W., Aifantis, K. E. & Fabry, B. Mechanical plasticity of cells. *Nat Mater* **advance online publication**, doi:10.1038/nmat4689
<http://www.nature.com/nmat/journal/vaop/ncurrent/abs/nmat4689.html#supplementary-information> (2016).
- 12 Trepaut, X., Deng, L., An, S. S., Navajas, D., Tschumperlin, D. J., Gerthoffer, W. T., Butler, J. P. & Fredberg, J. J. Universal physical responses to stretch in the living cell. *Nature* **447**, 592-595, doi:10.1038/nature05824 (2007).
- 13 Fabry, B., Maksym, G. N., Butler, J. P., Glogauer, M., Navajas, D. & Fredberg, J. J. Scaling the Microrheology of Living Cells. *Physical Review Letters* **87**, 148102, doi:10.1103/PhysRevLett.87.148102 (2001).

14 Kollmannsberger, P. & Fabry, B. Linear and Nonlinear Rheology of Living Cells. *Annual Review of Materials Research* **41**, 75-97, doi:10.1146/annurev-matsci-062910-100351 (2011).

15 Mongera, A., Pochitaloff, M., Gustafson, H. J., Stooke-Vaughan, G. A., Rowghanian, P., Kim, S. & Campàs, O. Mechanics of the cellular microenvironment as probed by cells *in vivo* during zebrafish presomitic mesoderm differentiation. *Nature Materials* **22**, 135-143, doi:10.1038/s41563-022-01433-9 (2023).

16 Mongera, A., Rowghanian, P., Gustafson, H. J., Shelton, E., Kealhofer, D. A., Carn, E. K., Serwane, F., Lucio, A. A., Giammona, J. & Campàs, O. A fluid-to-solid jamming transition underlies vertebrate body axis elongation. *Nature*, doi:10.1038/s41586-018-0479-2 (2018).

17 Sadeghipour, E., Garcia, M. A., Nelson, W. J. & Pruitt, B. L. Shear-induced damped oscillations in an epithelium depend on actomyosin contraction and E-cadherin cell adhesion. *eLife* **7**, e39640, doi:10.7554/eLife.39640 (2018).

18 Harris, A. R., Peter, L., Bellis, J., Baum, B., Kabla, A. J. & Charras, G. T. Characterizing the mechanics of cultured cell monolayers. *Proceedings of the National Academy of Sciences* **109**, 16449-16454, doi:10.1073/pnas.1213301109 (2012).

19 Streichan, S. J., Hoerner, C. R., Schneidt, T., Holzer, D. & Hufnagel, L. Spatial constraints control cell proliferation in tissues. *Proceedings of the National Academy of Sciences* **111**, 5586-5591, doi:10.1073/pnas.1323016111 (2014).

20 Rodríguez-Franco, P., Brugués, A., Marín-Llauradó, A., Conte, V., Solanas, G., Batlle, E., Fredberg, J. J., Roca-Cusachs, P., Sunyer, R. & Trepat, X. Long-lived force patterns and deformation waves at repulsive epithelial boundaries. *Nature Materials* **16**, 1029, doi:10.1038/nmat4972

<https://www.nature.com/articles/nmat4972#supplementary-information> (2017).

21 Lavi, Y., Sandler, Y., Saleem, A., Daraf, L., Nachum, S. & Atia, L. 3D-printed toolkit for regulating epithelial unjamming. *bioRxiv*, 2025.2011.2013.688246, doi:10.1101/2025.11.13.688246 (2025).

22 Sakaue-Sawano, A., Kurokawa, H., Morimura, T., Hanyu, A., Hama, H., Osawa, H., Kashiwagi, S., Fukami, K., Miyata, T., Miyoshi, H., Imamura, T., Ogawa, M., Masai, H. & Miyawaki, A. Visualizing Spatiotemporal Dynamics of Multicellular Cell-Cycle Progression. *Cell* **132**, 487-498, doi:<https://doi.org/10.1016/j.cell.2007.12.033> (2008).

23 Goldstien, L., Lavi, Y. & Atia, L. ConfluentFUCCI for fully-automated analysis of cell-cycle progression in a highly dense collective of migrating cells. *PLOS ONE* **19**, e0305491, doi:10.1371/journal.pone.0305491 (2024).

24 Liu, A. J. & Nagel, S. R. Nonlinear dynamics: Jamming is not just cool any more. *Nature* **396**, 21-22 (1998).

25 Sadati, M., Taheri Qazvini, N., Krishnan, R., Park, C. Y. & Fredberg, J. J. Collective migration and cell jamming. *Differentiation* **86**, 121-125, doi:10.1016/j.diff.2013.02.005 (2013).

26 Bi, D., Lopez, J. H., Schwarz, J. M. & Manning, M. L. A density-independent rigidity transition in biological tissues. *Nat Phys* **11**, 1074-1079, doi:10.1038/nphys3471

<http://www.nature.com/nphys/journal/v11/n12/abs/nphys3471.html#supplementary-information> (2015).

27 Bi, D., Yang, X., Marchetti, M. C. & Manning, M. L. Motility-Driven Glass and Jamming Transitions in Biological Tissues. *Physical Review X* **6**, 021011 (2016).

28 Atia, L., Fredberg, J. J., Gov, N. S. & Pegoraro, A. F. Are cell jamming and unjamming essential in tissue development? *Cells & Development*, 203727, doi:<https://doi.org/10.1016/j.cdev.2021.203727> (2021).

29 Park, J.-A., Atia, L., Mitchel, J. A., Fredberg, J. J. & Butler, J. P. Collective migration and cell jamming in asthma, cancer and development. *Journal of Cell Science*, doi:10.1242/jcs.187922 (2016).

30 DeCamp, S. J., Tsuda, V. M. K., Ferruzzi, J., Koehler, S. A., Giblin, J. T., Roblyer, D., Zaman, M. H., Weiss, S. T., Kılıç, A., De Marzio, M., Park, C. Y., Ogassavara, N. C., Mitchel, J. A., Butler, J. P. & Fredberg, J. J. Epithelial layer unjamming shifts energy metabolism toward glycolysis. *Scientific Reports* **10**, 18302, doi:10.1038/s41598-020-74992-z (2020).

31 De Marzio, M., Kılıç, A., Maiorino, E., Mitchel, J. A., Mwase, C., O'Sullivan, M. J., McGill, M., Chase, R., Fredberg, J. J., Park, J.-A., Glass, K. & Weiss, S. T. Genomic signatures of the unjamming transition in compressed human bronchial epithelial cells. *Science Advances* **7**, eabf1088, doi:doi:10.1126/sciadv.abf1088 (2021).

32 Park, J.-A., Kim, J. H., Bi, D., Mitchel, J. A., Qazvini, N. T., Tantisira, K., Park, C. Y., McGill, M., Kim, S.-H., Gweon, B., Notbohm, J., Steward Jr, R., Burger, S., Randell, S. H., Kho, A. T., Tambe, D. T., Hardin, C., Shore, S. A., Israel, E., Weitz, D. A., Tschumperlin, D. J., Henske, E. P., Weiss, S. T., Manning, M. L., Butler, J. P., Drazen, J. M. & Fredberg, J. J. Unjamming and cell shape in the asthmatic airway epithelium. *Nat Mater* **14**, 1040-1048 (2015).

33 Kim, J. H., Pegoraro, A. F., Das, A., Koehler, S. A., Ujwary, S. A., Lan, B., Mitchel, J. A., Atia, L., He, S., Wang, K., Bi, D., Zaman, M. H., Park, J.-A., Butler, J. P., Lee, K. H., Starr, J. R. & Fredberg, J. J. Unjamming and collective migration in MCF10A breast cancer cell lines. *Biochemical and Biophysical Research Communications* **521**, 706-715, doi:<https://doi.org/10.1016/j.bbrc.2019.10.188> (2020).

34 Mitchel, J. A., Das, A., O'Sullivan, M. J., Stancil, I. T., DeCamp, S. J., Koehler, S., Ocaña, O. H., Butler, J. P., Fredberg, J. J., Nieto, M. A., Bi, D. & Park, J.-A. In primary airway epithelial cells, the unjamming transition is distinct from the epithelial-to-mesenchymal transition. *Nature Communications* **11**, 5053, doi:10.1038/s41467-020-18841-7 (2020).

35 Garcia, S., Hannezo, E., Elgeti, J., Joanny, J.-F., Silberzan, P. & Gov, N. S. Physics of active jamming during collective cellular motion in a monolayer. *Proceedings of the National Academy of Sciences*, doi:10.1073/pnas.1510973112 (2015).

36 Palamidessi, A., Malinverno, C., Frittoli, E., Corallino, S., Barbieri, E., Sigismund, S., Beznoussenko, G. V., Martini, E., Garre, M., Ferrara, I., Tripodo, C., Ascione, F., Cavalcanti-Adam, E. A., Li, Q., Di Fiore, P. P., Parazzoli, D., Giavazzi, F., Cerbino, R. & Scita, G. Unjamming overcomes kinetic and proliferation arrest in terminally differentiated cells and promotes collective motility of carcinoma. *Nature Materials*, doi:10.1038/s41563-019-0425-1 (2019).

37 Malinverno, C., Corallino, S., Giavazzi, F., Bergert, M., Li, Q., Leoni, M., Disanza, A., Frittoli, E., Oldani, A., Martini, E., Lendenmann, T., Deflorian, G., Beznoussenko, G. V., Poulikakos, D., Ong, K. H., Uroz, M., Trepat, X., Parazzoli, D., Maiuri, P., Yu, W., Ferrari, A., Cerbino, R. & Scita, G. Endocytic reawakening of motility in jammed epithelia. *Nat Mater advance online publication*, doi:10.1038/nmat4848

<http://www.nature.com/nmat/journal/vaop/ncurrent/abs/nmat4848.html#supplementary-information> (2017).

38 Farhadifar, R., Roepert, J.-C., Algouy, B., Eaton, S. & Juelicher, F. The influence of cell mechanics, cell-cell interactions, and proliferation on epithelial packing. *Current Biology* **17**, 2095-2104, doi:10.1016/j.cub.2007.11.049 (2007).

39 Dow, L. P., Surace, S., Morozov, K., Kennedy, R. & Pruitt, B. L. Cyclic stretch regulates epithelial cell migration in a frequency dependent manner via intercellular vinculin recruitment. *npj Biological Physics and Mechanics* **1**, 2, doi:10.1038/s44341-024-00003-1 (2024).

40 Desai, L. P., White, S. R. & Waters, C. M. Cyclic Mechanical Stretch Decreases Cell Migration by Inhibiting Phosphatidylinositol 3-Kinase- and Focal Adhesion Kinase-mediated JNK1 Activation². *Journal of Biological Chemistry* **285**, 4511-4519, doi:<https://doi.org/10.1074/jbc.M109.084335> (2010).

41 Sanz-Moreno, V., Gadea, G., Ahn, J., Paterson, H., Marra, P., Pinner, S., Sahai, E. & Marshall, C. J. Rac Activation and Inactivation Control Plasticity of Tumor Cell Movement. *Cell* **135**, 510-523, doi:<https://doi.org/10.1016/j.cell.2008.09.043> (2008).

42 DiPersio, C. M. Double Duty for Rac1 in Epidermal Wound Healing. *Science's STKE* **2007**, pe33-pe33, doi:doi:10.1126/stke.3912007pe33 (2007).

43 Das, T., Safferling, K., Rausch, S., Grabe, N., Boehm, H. & Spatz, J. P. A molecular mechanotransduction pathway regulates collective migration of epithelial cells. *Nature Cell Biology* **17**, 276-287, doi:10.1038/ncb3115 (2015).

44 Hino, N., Rossetti, L., Marín-Llauradó, A., Aoki, K., Trepak, X., Matsuda, M. & Hirashima, T. ERK-Mediated Mechanochemical Waves Direct Collective Cell Polarization. *Developmental Cell* **53**, 646-660.e648, doi:<https://doi.org/10.1016/j.devcel.2020.05.011> (2020).

45 Aoki, K., Kondo, Y., Naoki, H., Hiratsuka, T., Itoh, R. E. & Matsuda, M. Propagating Wave of ERK Activation Orients Collective Cell Migration. *Developmental Cell* **43**, 305-317.e305, doi:10.1016/j.devcel.2017.10.016 (2017).

46 Atia, L., Bi, D., Sharma, Y., Mitchel, J. A., Gweon, B., A. Koehler, S., DeCamp, S. J., Lan, B., Kim, J. H., Hirsch, R., Pegoraro, A. F., Lee, K. H., Starr, J. R., Weitz, D. A., Martin, A. C., Park, J.-A., Butler, J. P. & Fredberg, J. J. Geometric constraints during epithelial jamming. *Nature Physics*, doi:10.1038/s41567-018-0089-9 (2018).

47 Lee, G., Atia, L., Lan, B., Sharma, Y., Nissim, L., Wu, M.-R., Pery, E., Lu, T. K., Park, C. Y., Butler, J. P. & Fredberg, J. J. Contact guidance and collective migration in the advancing epithelial monolayer. *Connective Tissue Research* **59**, 309-315, doi:10.1080/03008207.2017.1384471 (2017).

48 Schindelin, J., Arganda-Carreras, I., Frise, E., Kaynig, V., Longair, M., Pietzsch, T., Preibisch, S., Rueden, C., Saalfeld, S., Schmid, B., Tinevez, J.-Y., White, D. J., Hartenstein, V., Eliceiri, K., Tomancak, P. & Cardona, A. Fiji: an open-source platform for biological-image analysis. *Nature Methods* **9**, 676-682, doi:10.1038/nmeth.2019 (2012).

49 Davison, A. C. & Hinkley, D. V. *Bootstrap methods and their application*. (Cambridge University Press, 1997).

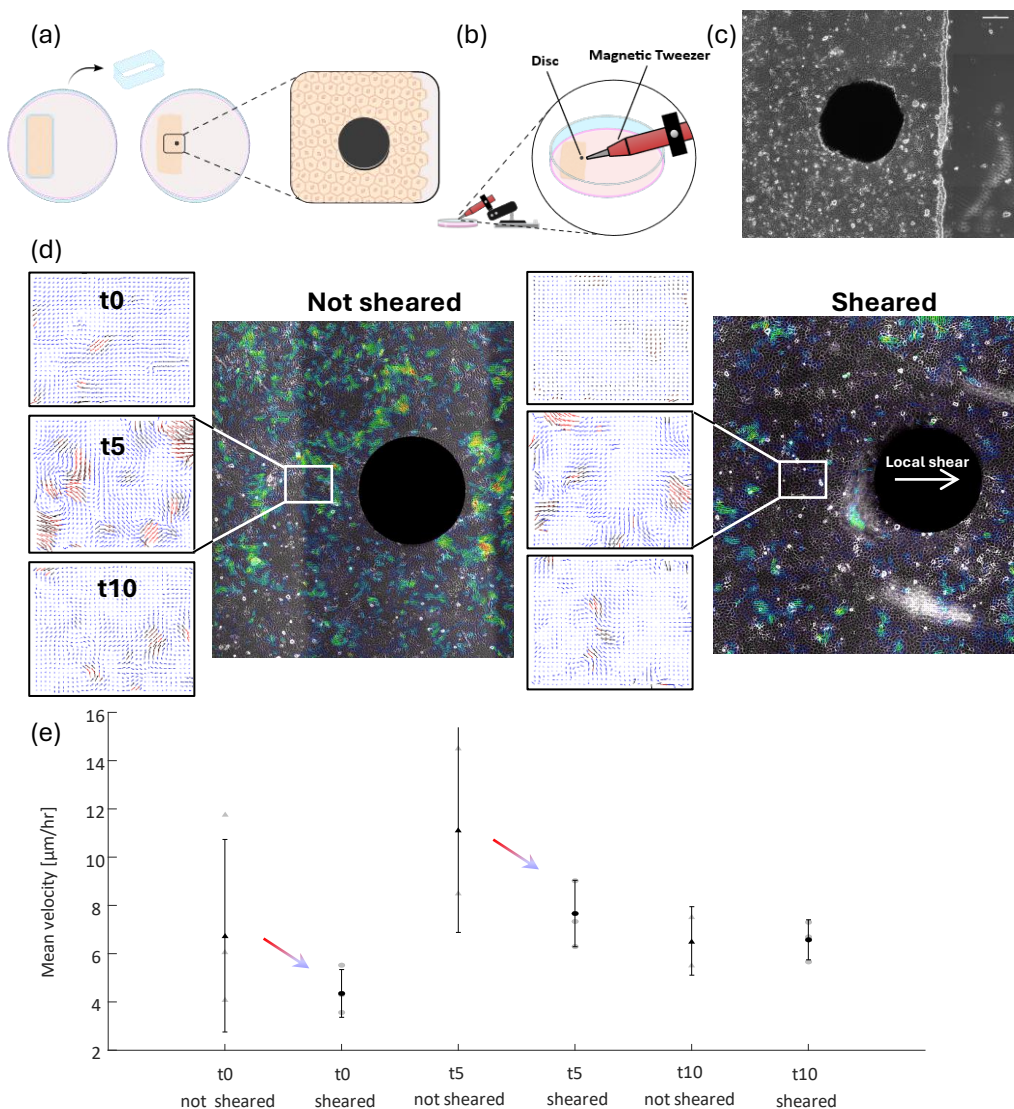


Figure 1. Local mechanical shear suppresses cellular dynamics many cell rows away from the site of perturbation. (a) Schematic of the epithelial experimental assay using MDCK cells cultured in ibidi wells (Methods). (b) Illustration of the experimental setup showing the magnetic tweezer and the attached magnetic disc (750 μm diameter, 500 μm height; Supplementary Fig. 1) used to apply localized shear stress (see Methods for force calibration; Supplementary Fig. 2). (c) Phase-contrast image of the epithelial monolayer with the magnetic disc in place (scale bar, 200 μm). (d) Representative PIV maps for sheared and not-sheared conditions (disc region was masked to reduce noise). The white rectangle marks the region of interest (ROI, 402 \times 332 μm) used for analysis. The right PIV maps are shown after 10s of magnetic force application for each maturation time, where t0 is defined as the time at which cells became fully confluent. (t0 = 20 hr, t5 = 25 hr, t10 = 30 hr; scale bar, 100 μm ; Supplementary Video 2). (e) Velocities across different maturation times (within the ibidi wells). Data were collected from three ROIs (the presented white rectangle, with two 2 more identical ROIs above and below it; 29X35 PIV grid) per condition across multiple independent plates: t0 sheared (n=3), t0 not sheared (n=3), t5 sheared (n=3), t5 not sheared (n=2), t10 sheared (n=3), and t10 not sheared (n=2). Time-lapse imaging was performed over 3–5 hours at 10-minute intervals. Plotted velocities are averaged across all three ROIs and throughout the entire time-lapse (as velocity traces showed no major temporal fluctuation (supplementary figure 3). All relevant comparisons between conditions were statistically significant (Mann–Whitney rank-sum test, $p \ll 0.005$; Supplementary Table 1).

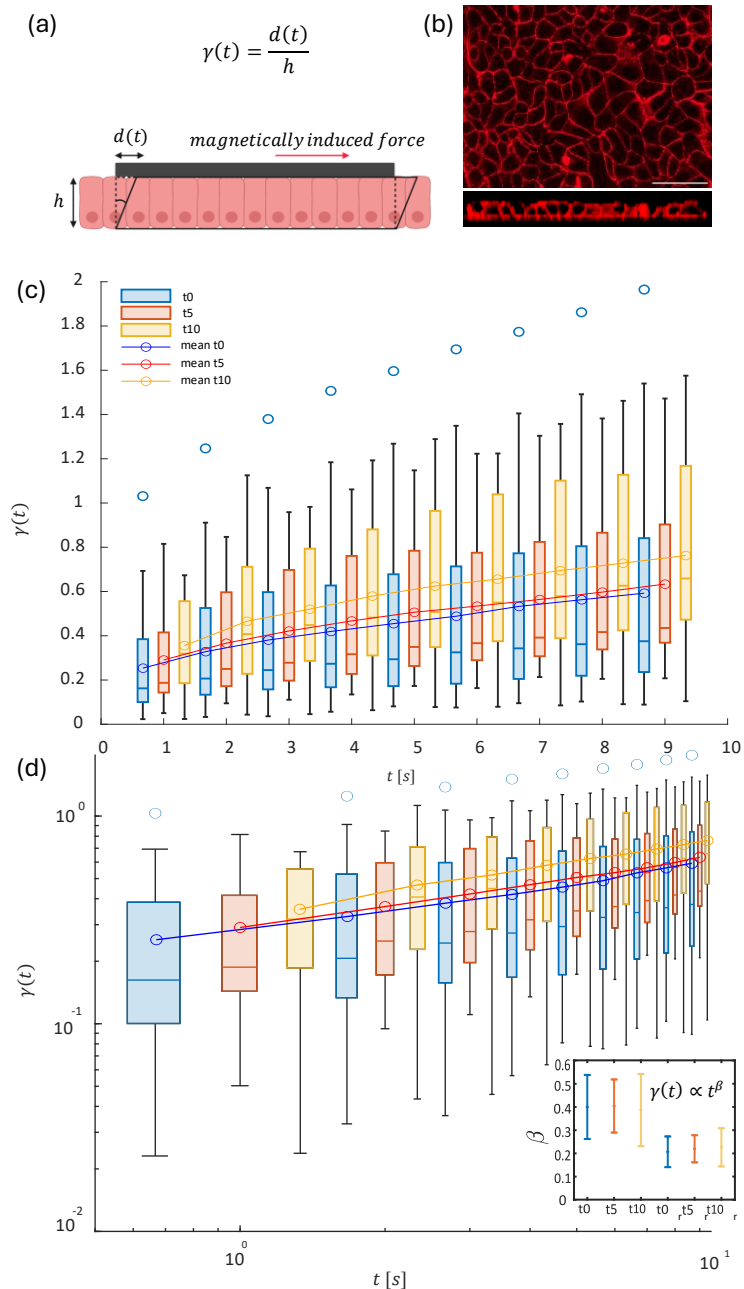


Figure 2. Shear strain measurements reveal how, during maturation, the tissue softens. (a) Schematic of the tissue shear model used to assess shear strain. (b) Fixed and stained epithelial monolayers used to assess the tissue height (scale bar, 50 μ m; see Methods). (c) Boxplot of shear strain distributions across maturation stages, obtained from independent experiments: t0 (n=30); t5 (n=14); t10 (n=27) (Supplementary Fig. 5). Boxplots display the median (horizontal line inside each box), the mean (circle), and the mean trend (connected line across means). Boxes indicate the interquartile range. (d) Boxplot of the log-log-transformed data. The inset shows β values extracted from power-law fits to the shear strain curves, shown for each maturation stage. r denotes recovery. Error bars represent standard deviation. Statistical comparisons were performed using the Mann-Whitney rank-sum test (Supplementary Table 1).

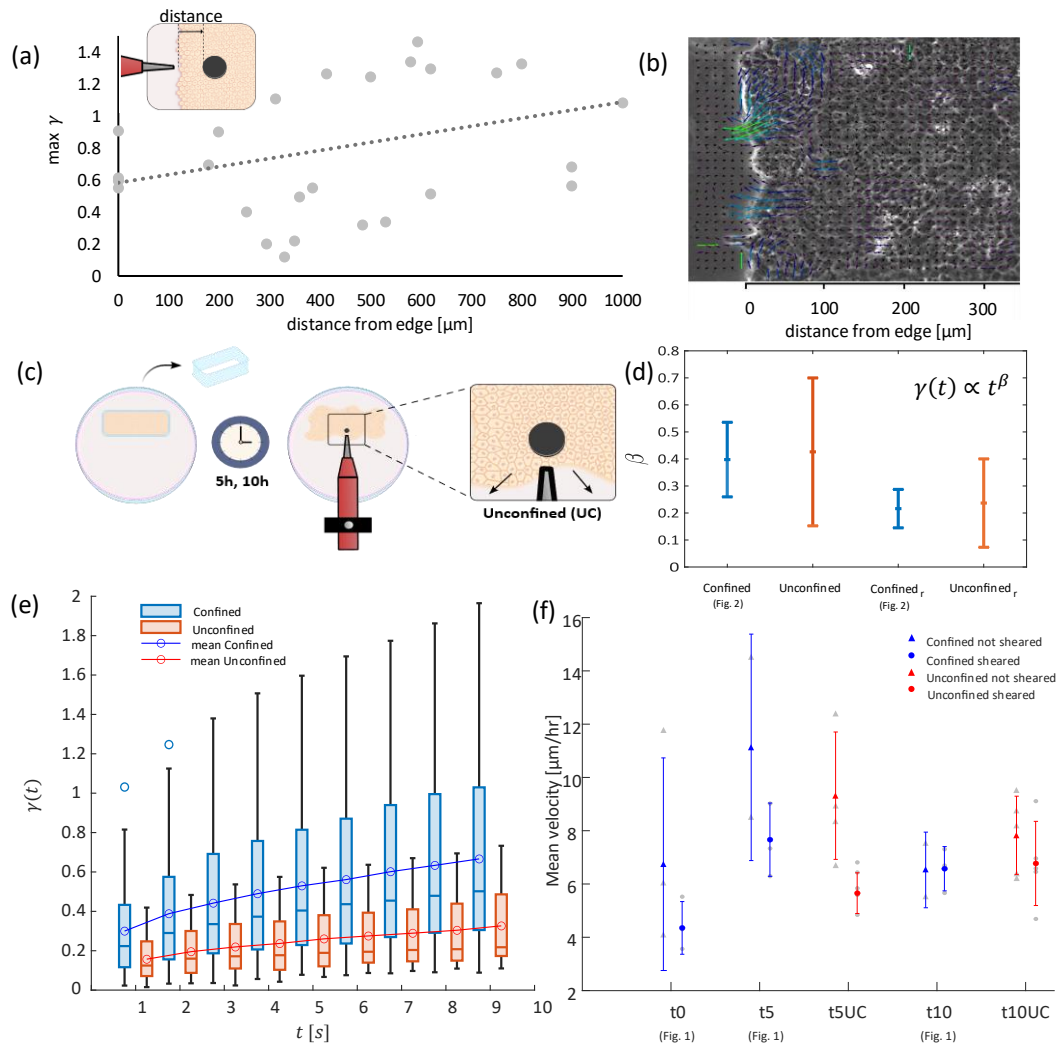


Figure 3. Unconfinement increases tissue dynamics and stiffness, and enables the propagation of mechanical shear signals. (a) The maximum shear strain γ as a function of the disc's distance from the tissue edge. Data were obtained from confined t10 experiments ($n = 27$). Pearson correlation analysis $r = 0.399$. (b) PIV analysis at the tissue edge, demonstrating elevated cellular motility near the edge. (c) Schematic of the Unconfined (UC) experimental assay. Culture well is removed after 20 hours, upon reaching confluence. (d) β values extracted from power-law fits of shear strain curves for each condition (Confined and Unconfined), where r denotes recovery. (e) Comparison of shear strain over time between Unconfined and Confined Independent experiments: t5 UC ($n = 10$); t10 UC ($n = 13$). Boxplots represent shear strain distributions for each condition, and display the median (horizontal line inside each box), the mean (circle), and the mean trend (connecting line across means). Boxes indicate the interquartile range. (f) Mean velocity over time for each condition; red represents Unconfined experiments, blue represents the Confined data as shown in Figure 1. UC Data were collected from 3 ROIs (29X35 Grid) per condition across multiple independent plates: t5 UC sheared ($n = 5$), t5 UC not sheared ($n = 4$), t10 UC sheared ($n = 5$), and t10 UC not sheared ($n = 5$). All relevant statistical comparisons between conditions showed a significant statistical difference as calculated by the Mann-Whitney rank-sum test, $p < 0.005$ (Supplementary Table 1).

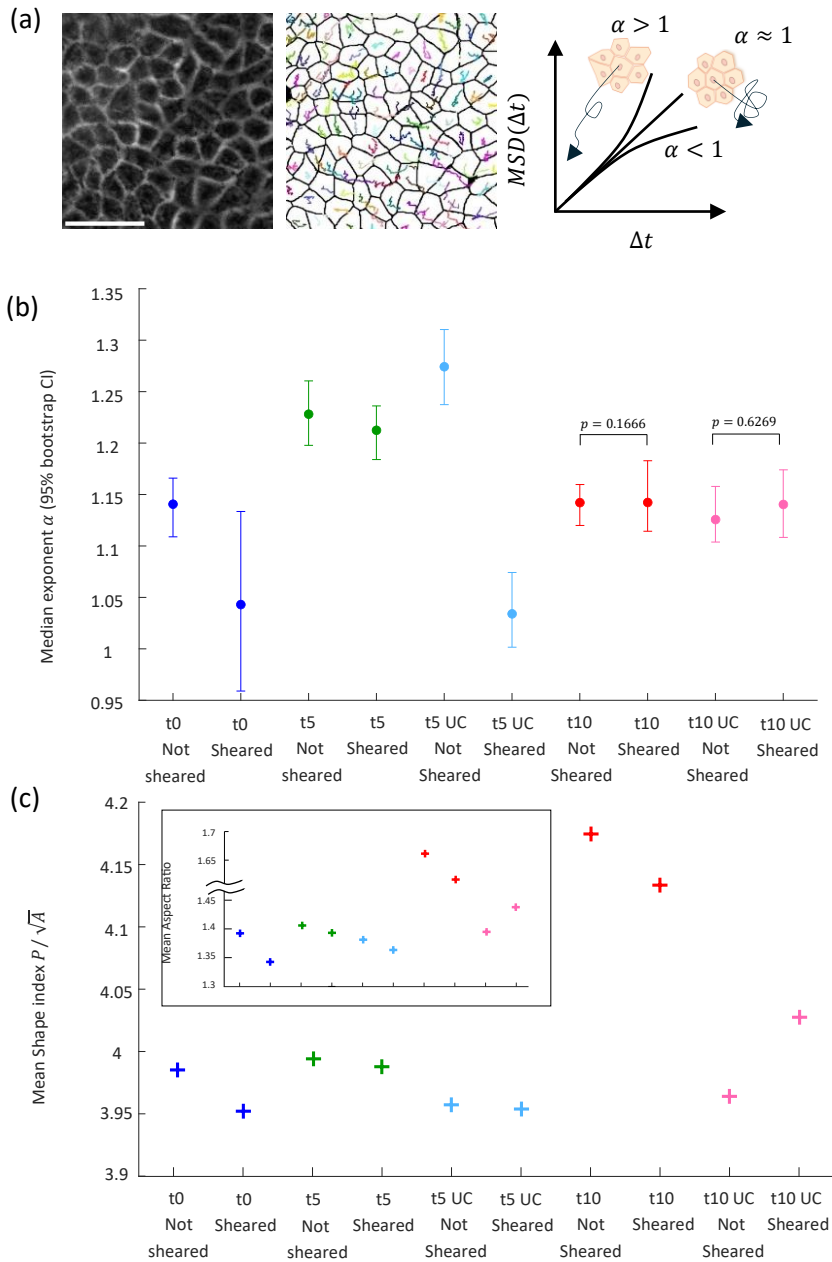
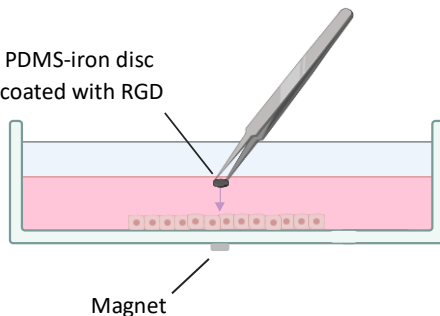
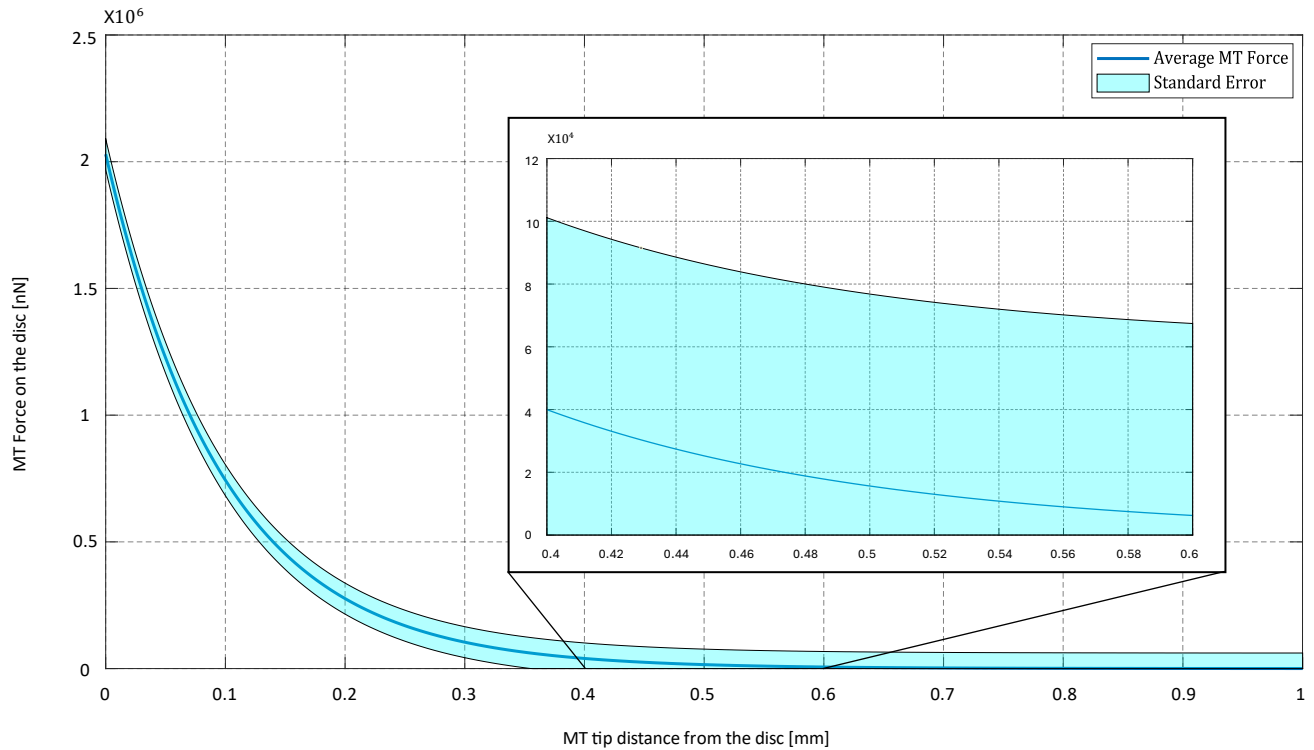


Figure 4. Shear-induced migratory suppression partially coincides with epithelial jamming metrics. (a) Phase-contrast image of the region of interest (scale bar, 100 μ m) used for velocity analysis (left), corresponding cell segmentation generated using Cellpose (see Methods), and individual cell tracks (see Methods; middle) and illustrating caging dynamics as portrayed by exponent α (right). (b) Median of the α values obtained from the power-law model ($MSD(\Delta t) = A\Delta t^\alpha$) fit for each track. Outliers of negative α , and $\alpha > 2$ values were filtered out. Time-lapse imaging was performed for 3 hours at 10-minute intervals. t0 sheared (n=3, 4 ROIs in total with 406 Average number of cells); t0 not sheared (n=3, 9 ROIs with 2077 Avg.); t5 sheared (n=4, 12 ROIs with 3051 Avg.); t5 not sheared (n=1, 3 ROIs with 1208 Avg.); t5 UC sheared (n=5, 13 ROI total with 1812 Avg.); t5 UC not sheared (n=2, 5 ROI total with 1453 Avg.); t10 sheared (n=1, 3 ROI with 1785 Avg.); t10 not sheared (n=2, 6 ROI total with 3230 Avg.); t10 UC sheared (n=3, 7 ROI total with 1650 Avg.); t10 UC not sheared (n=4, 11 ROI total with 2242 Avg.). Number of MSD curves for each condition: t0 not sheared (n=2379); t0 sheared (n=407); t5 not sheared (n=1547); t5 sheared (n=3918); t5 UC not sheared (n=1916); t5 UC sheared (n=2344); t10 not sheared (n=3619); t10 sheared (n=1934); t10 UC not sheared (n=3319); t10 UC sheared (n=2454). All relevant statistical comparisons between conditions showed a significant statistical difference as calculated by the Mann-Whitney rank-sum test, except the t10 and t10 UC pairs. (Supplementary Table 1). (c) Mean cell shape ($Cell\ Perimeter/\sqrt{Cell\ Area}$) and aspect ratio ($Long\ major\ axis/short\ major\ axis$) for each experimental condition. Calculations are based on the same segmented cell data used for the MSD analysis.

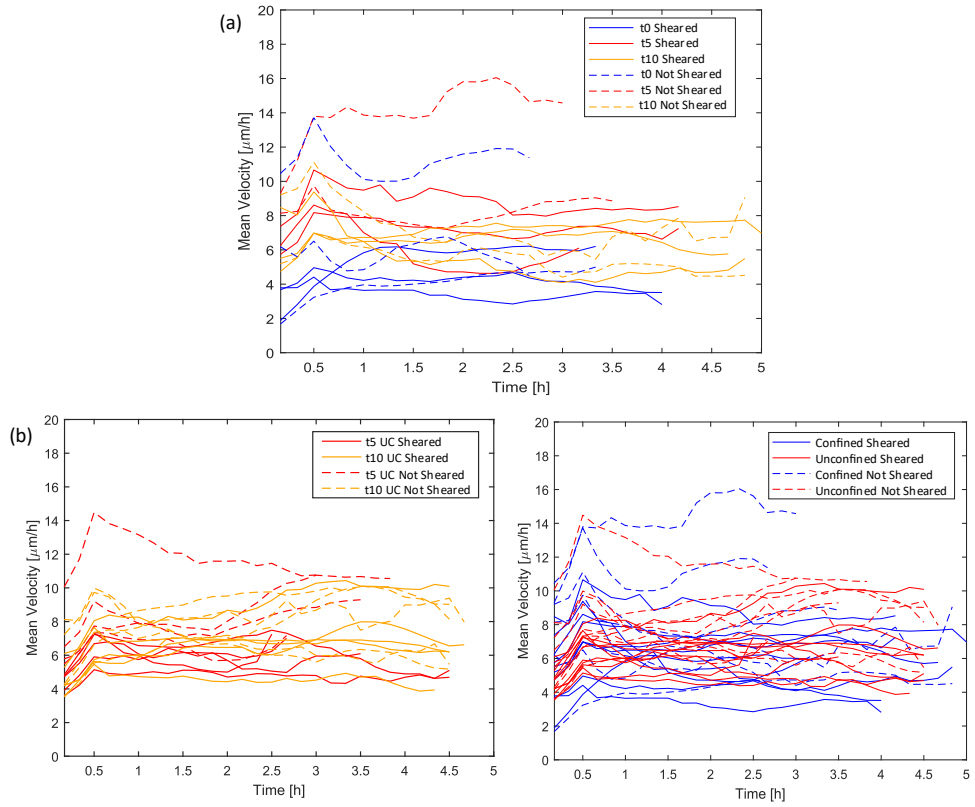
Supplementary Information



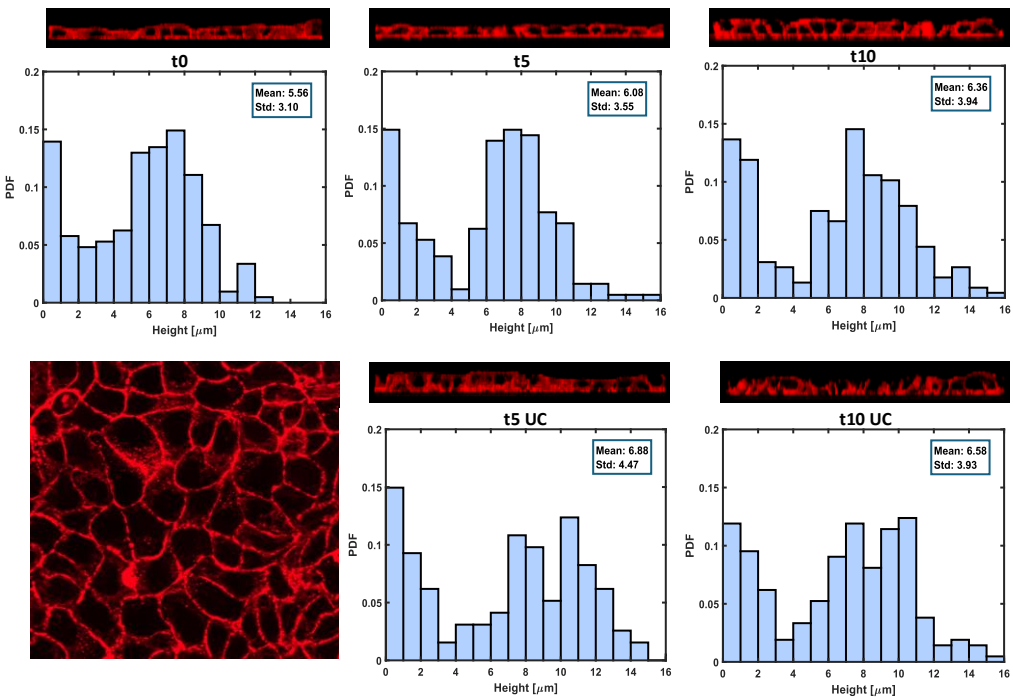
Supplementary Figure 1. Magnetic disc placements. Illustration of the method used to position the magnetic disc on the tissue, using tweezers and a magnet below the dish (Methods). The disc surface was activated with Sanpah and coated with RGD peptide that adheres to the cells.



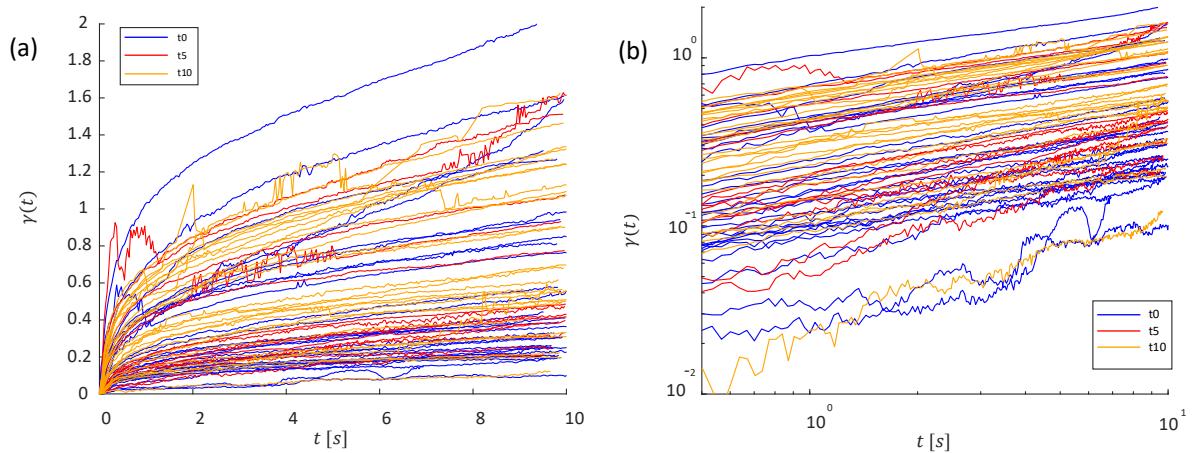
Supplementary Figure 2. Force calibration. Average force exerted on the magnetic disc in MDCK shear experiments as a function of distance from the magnetic tweezer (MT) over the full 0–1 mm range. Inset: The average force within the 0.4–0.6 mm range. 500 μ m distance between the MT and the magnetic disc produces a force of $\sim 2 \cdot 10^4$ [nN].



Supplementary Figure 3. Mean velocity over time across maturation times. (a) Mean velocity curves over time for different maturation times. (b) (Left) Mean velocity curves over time for different maturation stages in the Unconfined experiments. (Right) Comparison of mean velocity over time between Confined and Unconfined experiments.



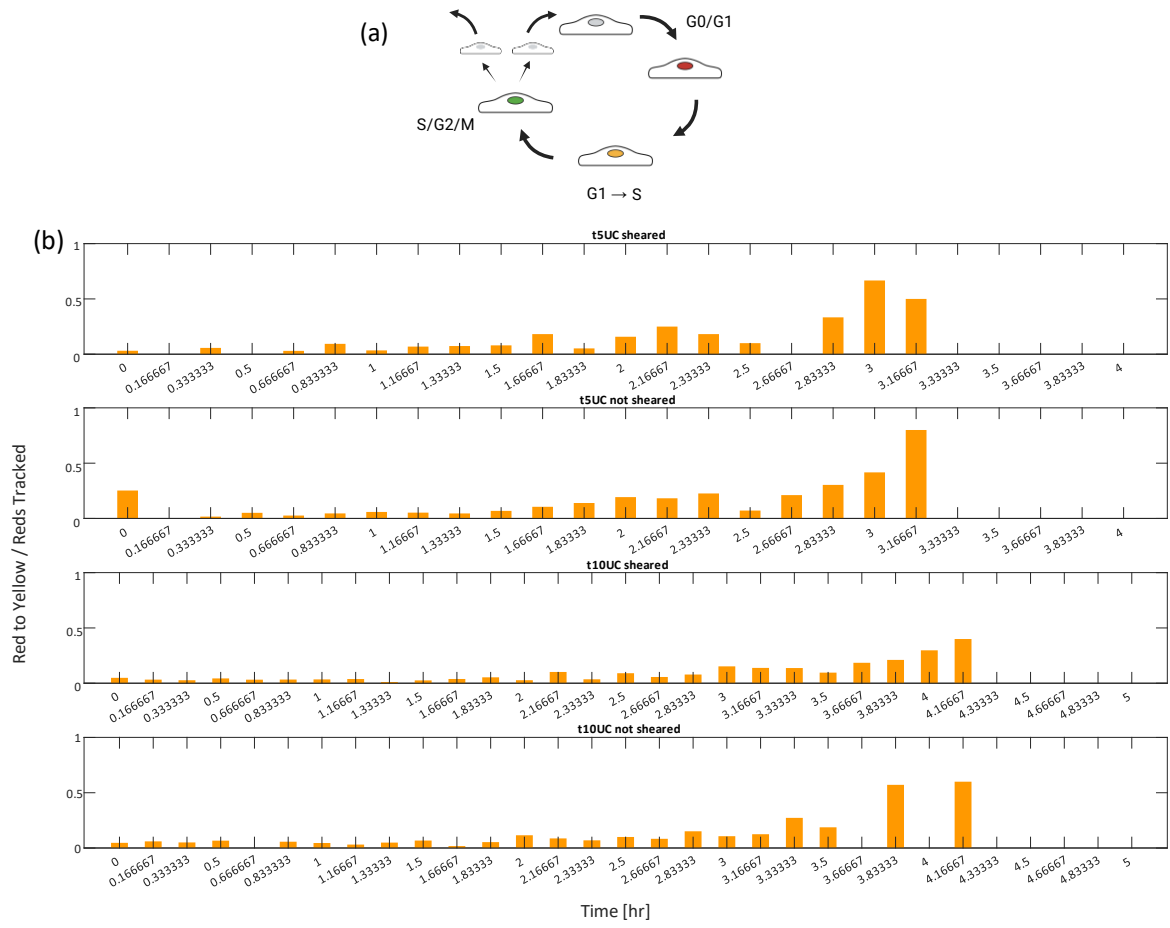
Supplementary Figure 4. Tissue height measurements. Fixed and stained epithelial monolayers were used to measure cell height across experimental conditions (t0, t5, t5UC, t10, t10UC). Probability density functions (PDFs) of cell height are shown for each condition, along with corresponding mean and standard deviation values.



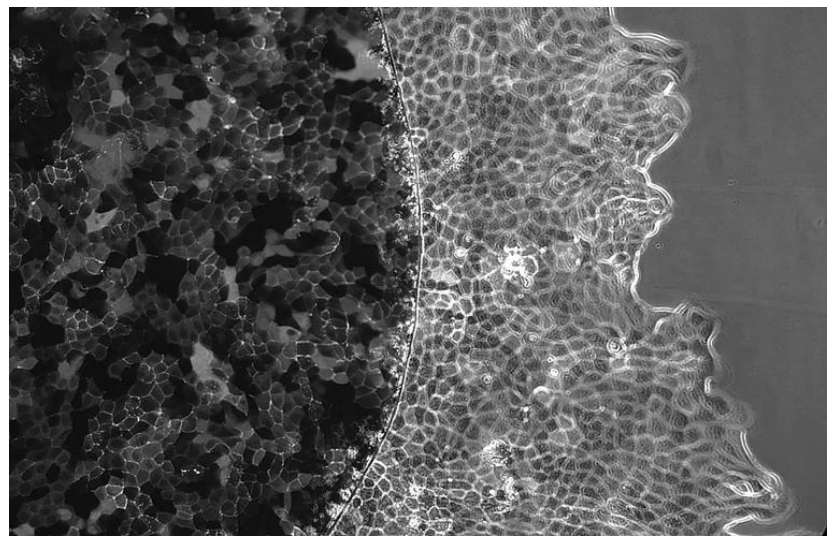
Supplementary Figure 5. Shear strain curves from the independent experiments, divided to maturation groups: t0 ($n = 30$), t5 ($n = 14$), and t10 ($n = 27$). Panels show (a) regular scale, (b) log–log scale.

Mean Velocity comparison	Condition	Frame 1	Frame 4	Frame 7	Frame 10	Frame 13	Frame 18			
Sheared vs Not Sheared										
Fig. 1	t0	0	2.65*10^-223	9.95*10^-27	0	9.97*10^-253	4.05*10^-7			
	t5	0	1.90*10^-72	4.86*10^-252	1.59*10^-264	0	2.84*10^-34			
	t10	3.86*10^-149	2.35*10^-20	0.00027	3.95*10^-7	4.11*10^-39	3.48*10^-14			
Fig. 3	t5UC	0	5.56*10^-85	0	2.09*10^-161	0	6.31*10^-301			
	t10 UC	0.00286	1.50*10^-52	5.14*10^-195	0	1.80*10^-193	2.28*10^-78			
Sheared										
Fig. 1	t0 vs t5	0	0	0	0	7.51*10^-190	0			
	t0 vs t10	0	0	4.33*10^-149	0	3.92*10^-281	1.31*10^-232			
	t5 vs t10	5.26*10^-53	7.35*10^-34	1.57*10^-57	1.04*10^-14	7.52*10^-7	9.91*10^-71			
Fig. 3	t5UC vs t10UC	3.65*10^-106	5.76*10^-14	0.001935	5.49*10^-22	1.75*10^-11	0.007485			
Not Sheared										
Fig. 1	t0 vs t5	0	1.53*10^-285	0	2.62*10^-77	0	3.17*10^-206			
	t0 vs t10	2.79*10^-96	2.35*10^-134	9.32*10^-63	1.93*10^-86	2.53*10^-34	3.60*10^-38			
	t5 vs t10	1.69*10^-117	2.43*10^-62	0	4.15*10^-256	0	3.06*10^-175			
Fig. 3	t5UC vs t10UC	1.15*10^-319	7.97*10^-38	2.50*10^-95	3.00*10^-107	6.17*10^-13	1.74*10^-118			
Shear Strain comparison	Condition	1s	2s	3s	4s	5s	6s	7s	8s	9s
Fig. 2	t0 vs t5	0.44217	0.35772	0.37105	0.27304	0.22168	0.2957	0.31836	0.34415	0.35753
	t0 vs t10	0.02182	0.02798	0.03159	0.02473	0.02182	0.02578	0.05934	0.06628	0.06158
	t5 vs t10	0.24263	0.30255	0.30255	0.27749	0.28984	0.26551	0.30255	0.26551	0.22117
Fig. 3	t5UC vs t10UC	0.9737	0.9737	0.92121	0.92121	0.92121	1	0.86907	1	0.86026
	C vs UC	0.00369	0.00235	0.00115	0.00071	0.00060	0.00056	0.00036	0.00025	0.00046
β comparison		Shear		Recovery			Shear vs Recovery			
Fig. 2	t0 vs t5	0.75278		t0 vs t5	0.73629		t0	8.89*10^-11		
	t0 vs t10	0.31017		t0 vs t10	0.49319		t5	1.39*10^-5		
	t5 vs t10	0.30255		t5 vs t10	0.84458		t10	1.52*10^-7		
Fig. 3	C vs UC	0.50639		C vs UC	0.89007		C	3.94*10^-21		
							UC	0.00027		
values from α MSD fit	Sheared vs Not Sheared	t0	t5	t5UC	t10	t10UC				
Fig. 4		0.0143	0.0527	2.23*10^-26	0.1666	0.6269				

Supplementary Table 1. P-Value Tables. Velocity means comparison test results (1st). Shear Strain comparison test results (2nd); β comparison test results (3rd); α comparison test results (4th). All p-values were calculated using Mann-Whitney rank-sum tests.

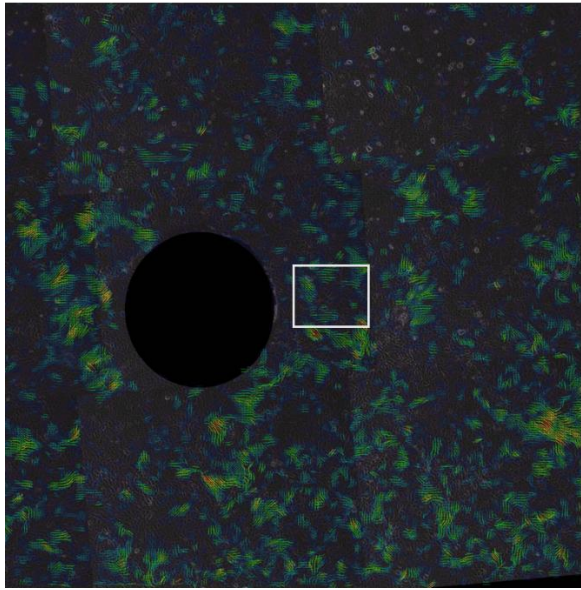


Supplementary Figure 6. Fucci cell cycle progression analysis for Unconfined experiments. (a) Cell-Cycle illustration. (b) The fraction of cells transitioning to S-phase (yellow/green) divided by G1-phase (red) cells is shown for each UC condition: t5, t10, t5 not sheared, and t10 not sheared. Transitions were counted at the last frame in which the cell appeared red.

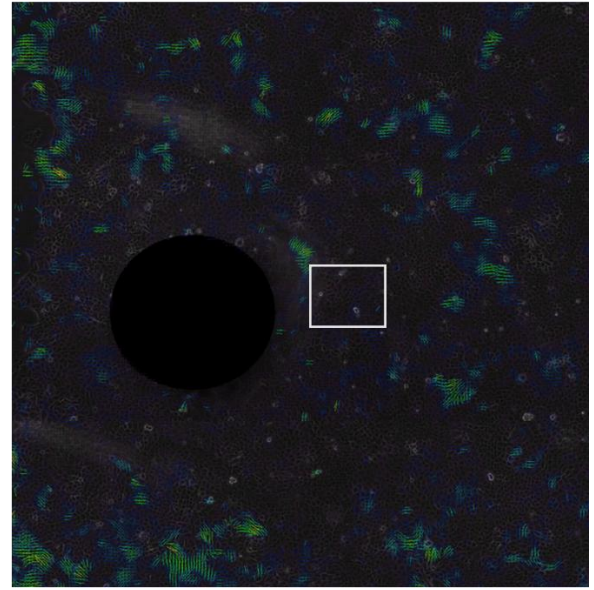


Supplementary Video 1. magnetic shear and recovery. A close-up of the magnetic disc and underlying cells during a 10-second force application followed by a 10-second recovery, visualized using ZO-1 GFP fluorescence markers.

not sheared



sheared



Supplementary Video 2. Velocity field around the magnetic disc in sheared and not sheared tissues.
Representative image velocimetry maps showing a wide region of the tissue surrounding the magnetic disc, under two conditions: sheared and not sheared. The white rectangle indicate the region of interest (ROI) used for quantifying mean velocity.